Article

Site-Specific Cryo-focused Ion Beam Sample Preparation Guided by 3D Correlative Microscopy

Jan Arnold,[1] Julia Mahamid,[1,*] Vladan Lucic,[1] Alex de Marco,[2] Jose-Jesus Fernandez,[3] Tim Laugks,[1] Tobias Mayer,[2] Anthony A. Hyman,[4] Wolfgang Baumeister,[1] and Jürgen M. Plitzko[1,*]

[1]Department of Molecular Structural Biology, Max Planck Institute of Biochemistry, Martinsried, Germany; [2]FEI Company, Graefelfing, Germany; [3]Centro Nacional de Biotecnologia, Madrid, Spain; and [4]Max Planck Institute of Molecular Cell Biology and Genetics, Dresden, Germany

ABSTRACT   The development of cryo-focused ion beam (cryo-FIB) for the thinning of frozen-hydrated biological specimens enabled cryo-electron tomography (cryo-ET) analysis in unperturbed cells and tissues. However, the volume represented within a typical FIB lamella constitutes a small fraction of the biological specimen. Retaining low-abundance and dynamic subcellular structures or macromolecular assemblies within such limited volumes requires precise targeting of the FIB milling process. In this study, we present the development of a cryo-stage allowing for spinning-disk confocal light microscopy at cryogenic temperatures and describe the incorporation of the new hardware into existing workflows for cellular sample preparation by cryo-FIB. Introduction of fiducial markers and subsequent computation of three-dimensional coordinate transformations provide correlation between light microscopy and scanning electron microscopy/FIB. The correlative approach is employed to guide the FIB milling process of vitrified cellular samples and to capture specific structures, namely fluorescently labeled lipid droplets, in lamellas that are 300 nm thick. The correlation procedure is then applied to localize the fluorescently labeled structures in the transmission electron microscopy image of the lamella. This approach can be employed to navigate the acquisition of cryo-ET data within FIB-lamellas at specific locations, unambiguously identified by fluorescence microscopy.

INTRODUCTION

Cellular cryo-electron tomography (cryo-ET) is a method for three-dimensional (3D) imaging of pleomorphic cellular structures (1). Vitrification arrests cells in a close-to-native state (2) and cryo-tomograms under such conditions capture snapshots of molecular landscapes inside the cells at the time of freezing (3). Practically, cellular samples up to 500 nm in thickness can be imaged by cryo-ET, but the signal-to-noise ratio (SNR) of the images drops considerably beyond 300 nm. The development of cryo-focused ion beam (cryo-FIB) milling enables cryo-ET analysis on native cells and tissues, by producing distortion-free, electron-transparent lamellas thinner than 300 nm (4–7). However, the volume retained within a typical lamella constitutes a small fraction of the cell. This fact necessitates the introduction of correlative light and electron microscopy (CLEM) in 3D with the aim of guiding the FIB milling process and to capture unique and transient structures within lamellas, to be subsequently studied by cryo-ET.

CLEM methods combine the possibility of analyzing the dynamics and localization of fluorescently labeled molecules using fluorescent light microscopy (FLM), together with the high-resolution view of cellular morphology and macromolecular ultrastructure obtainable with different modalities of electron microscopy (EM). One modality of CLEM aiming at high-resolution studies of macromolecular complexes, typically involves fluorescence imaging of thin frozen-hydrated specimens after vitrification using cryo-FLM (8,9). Features of interest are localized on a 3 mm transmission electron microscopy (TEM) grid and the coordinates are then transferred directly from the light microscope to the TEM for cryo-ET. To perform cryo-CLEM, it is required that the sample after vitrification is kept at temperatures below −140°C to maintain the vitreous state of the water. Moreover, the sample must be shielded from the surrounding atmosphere to prevent deposition of frost caused by environmental humidity. To achieve high-localization accuracy in two dimensions (2D) and 3D, cryo-FLM must be performed with sufficient thermal and mechanical stability. So far, a number of cryo-stages and strategies have been successful at applying cryo-CLEM in 2D (7,9–14). However, the limited numerical aperture (NA) of the objective lens is a crucial factor determining sensitivity and resolution of the FLM observation, and except for an approach where the complete microscope is kept below −140°C (15), only air objectives with a long working distance and consequently low NA are used in cryo-FLM. Accurate localization of fluorescent features can nevertheless be achieved using fiducial markers.

These are subdiffraction-limit objects that can be visualized in both FLM and TEM. Image transformations are calculated based on the coordinates of the markers in both imaging modalities to account for scaling, rotation, and translations. Geometrical distortions because of mechanical deformation and the movement of cellular components are negligible at cryogenic conditions, thus the specimen can be treated as a rigid body to calculate the transformations. Fiducial-based correlation allowed for the identification of fluorescent features in the TEM in 2D with an accuracy better than 100 nm (11,12). In this study, we present the development of a cryo-stage, which allows the use of a standard air objective with a short working distance of 410 μm and 0.9 NA to acquire spinning-disk confocal stacks of fluorescently labeled objects in vitrified samples. We identified suitable fiducials, namely magnetic beads discernable both in FLM and scanning electron microscopy (SEM)/FIB, and developed computational methodologies for 3D coordinate transformation to achieve correlation between FLM and SEM/FIB data. The developed procedure is used to guide FIB milling of fluorescently labeled lipid droplets in HeLa cells using established workflows for cellular sample preparation (Table S1 in the Supporting Material). The correlation procedure is then employed to unambiguously localize the fluorescent features within the FIB lamella with the aim of navigating data acquisition by cryo-ET.

MATERIALS AND METHODS

HeLa cell culture and vitrification

Wild-type HeLa cells were cultured in Dulbecco's modified Eagle's medium supplemented with 10% fetal bovine serum and 2 mM l-glutamine and maintained using standard procedures in an incubator at 37°C and 5% CO_2. Cell-cycle synchronization was achieved by a double block using 2 mM thymidine (Sigma-Aldrich Chemie, Munich, Germany) for 18 h, release for 6 h, followed by a second block using 2 μm S-Trityl-L-Cysteine (Enzo Life Sciences, Lörrach, Germany) for 8 h. BODIPY fluorescent dyes (Life Technologies-Thermo Fischer Scientific, Waltham, MA) for labeling of lipid droplets were added to the culture and incubated for 5 min at 37°C (BODIPY 493/503: green fluorescence, general neutral lipid stain; BODIPY 558/568 C12: red fluorescence neutral fatty acids). Mitotic cells were detached from the culture flask by mechanical shake off, and the collected medium was centrifuged at 300 g for 2 min to concentrate the cell pellet. Holey carbon-coated 200 mesh copper grids (Quantifoil Micro Tools (Jena, Germany): R 2/1) were preincubated with 2 μl of a mixture of 1 μm Dynabeads (Life Technologies-Thermo Fischer Scientific: MyOne with 40% iron oxide, carboxylic acid) diluted 1:10 from original stock and 200 nm Tetraspeck (Life Technologies-Thermo Fischer Scientific) diluted 1:100. Four microliters of the cell suspension was deposited onto the grids. Grids were blotted from the reverse side and immediately plunged into a liquid ethane/propane mixture at liquid nitrogen temperature using a Vitrobot Mark 4 (FEI Company, Eindhoven, The Netherlands). The Vitrobot was set to 37°C, 90% humidity, blot force 10, and blot time of 10 s and 2 s drain time. The frozen grids were stored in sealed boxes in liquid nitrogen until further processing.

Cryo-fluorescent light microscopy

Frozen grids were clipped into autogrid specimen cartridges modified for FIB preparation under shallow angles (7) and mounted into a shuttle system (Figs. 1 and S1). Grids were imaged by light microscopy using the FEI Corr-

Sight microscope equipped with a CorrSight Cryo-Module (cryo-stage) developed and prototyped together with FEI Company (Fig. 1). The microscope includes a wide-field light path and a spinning-disk confocal path with independent light sources. The spinning-disk confocal is equipped with a laser light source, which emits at four channels (405/488/561/640 nm) and passes through an FEI spinning-disk confocal setup, and a 1344 × 1024 pixel camera with a pixel size of 6.4 μm (Hamamatsu Photonics Deutschland, Herrsching am Ammersee, Germany: Digital Camera C10600 ORCA-R2). Zeiss Plan-ApoChromat (Carl Zeiss, Oberkochen, Germany) air objectives with 5×/0.16 NA and 20×/0.8 NA air objectives were used for obtaining overviews of the sample with transmitted light. Data acquisition used for 3D correlation was done with a Zeiss EC Plan-Neofluar 40×/0.9 NA Pol (working distance = 410 μm) air objective corrected for 170 μm cover glass thickness. The combination of the camera's physical pixel size with the 40× objective resulted in an image pixel size of 161.25 nm. The resolution of the system was determined with point-spread-function (PSF) measurements on 200 nm diameter fluorescent beads. For the green fluorescence channel (λ = 488 nm), the determined resolution is the following: x = 580 nm; y = 570 nm; z = 2 μm (parallel to the optical path). The PSF is practically identical for all channels because the performance is limited by the wavelength-independent optical settings of our system rather than by the Abbe diffraction limit. Drift in a thermally equilibrated system was measured to 100 nm/min at cryogenic temperatures. Image acquisition was done using FEI MAPS 2.1 software, operated in semiautomated mode to generate montages of the grids and in batch mode for the acquisition of spinning-disk confocal stacks at multiple areas of interest. Spinning-disk illumination was preferred because parallel scanning of a sample is faster compared with raster/line scanning systems.

Cryo-SEM/FIB and lamella milling

Grids were removed from the CorrSight shuttle, mounted into a FIB-shuttle (7), and transferred into a dual-beam (SEM/FIB) microscope (Quanta 3DFEG, FEI Company) using a cryo-transfer system (PP3000T, Quorum Technologies, Laughton, Lewes, East Sussex, Great Britain). During FIB operation, samples were kept at constant liquid nitrogen temperature using an in-house designed rotatable cryo-stage (16). To improve sample conductivity for correlation in cellular samples, the grids were first sputtered with platinum (10 mA, 30 s) in the Quorum prep-chamber. The MAPS software installed on the dual-beam microscope provides three-point correlation between the cryo-FLM and cryo-SEM images and was used for initial 2D navigation. SEM and FIB images of areas of interest, previously identified in the FLM data, were acquired at a stage tilt at which milling is latter performed. The images were acquired at a magnification providing the same field of view as in the FLM data, to allow identification of fiducial markers. SEM micrographs were acquired at 10 kV and 42 pA using a secondary electron (SE) detector and a back-scattered electron detector (EBSD). FIB images were produced at 30 kV and 10 pA using the SE detector. Three-dimensional correlation was performed at this point. For lamella preparation at areas of interest after correlation, the samples were coated with a protective layer of organometallic platinum using the in situ gas injection system (GIS, FEI Company) operated at room temperature, with a stage working distance of 12 mm and a gas injection time of 5 s. Lamellas were prepared using the Gallium ion beam at 30 kV at stage tilt angles of 15° to 25°. Lamella preparation was conducted in a stepwise scheme: rough milling with high currents of 0.5 nA followed by lowered currents, down to 50 pA for the final cleaning step. Progress of the milling process was monitored using the SEM SE signal until a final lamella thickness of ~300 nm was obtained.

Cryo-TEM

Cryo-TEM observations were performed on a Titan Krios transmission electron microscope (FEI Company) operated at 300 kV, a GIF post-column energy filter (Gatan, Pleasanton, CA), and a 3838 × 3710 K2 Summit direct detection camera (Gatan). Montage imaging of the lamellas was acquired at
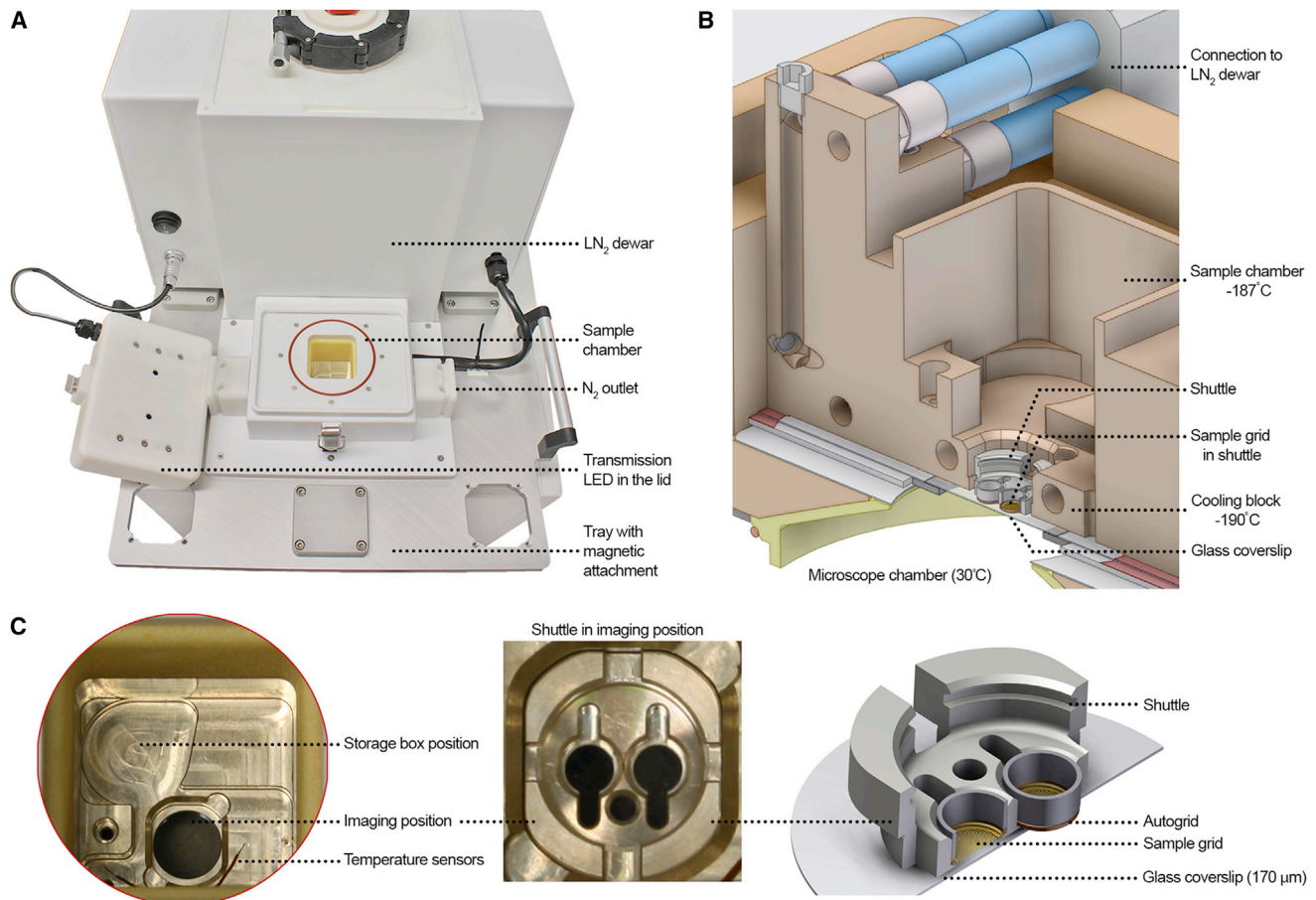
FIGURE 1   Design of cryo-stage and shuttle system. (*A*) FEI CorrSight Cryo-Module (cryo-stage). (*B*) Schematic representation of the cryo-stage in cross sections. (*C*) Left: magnified view of the sample chamber. Center: shuttle in imaging position. Right: schematic representation of the magnified shuttle with samples in autogrids. Distance between vitrified sample and glass cover slip is 200 μm.

a pixel size of 2.28 nm, controlled by SerialEM software under low-dose conditions (17). High-magnification images were acquired at a pixel size of 0.342 nm and an electron dose of 10 e⁻/Å².

of 0.342 nm and an electron dose of 10 $e^-/Å^2$.

Software

Image acquisition on the FEI CorrSight was done with MAPS 2.1 software (FEI Company). The light microscope image preprocessing and SEM/FIB 2D marker picking was done with FIJI (Fiji Is Just ImageJ, version 1.49g) (18) and the 3D Object Counter plugin for ImageJ by Fabrice P. Cordelieres and Daniel White to obtain the fiducial coordinates from the confocal data (19). Custom-made software in Python based on sequential least squares programming as implemented in SciPy package was used for calculating the coordinate based transformation (20). TOM Toolbox (https://www.biochem.mpg.de/tom) was used for spatial transformations inside MATLAB (The MathWorks, Natick, MA).

RESULTS

Experimental setup

Fluorescent light microscopy

The newly developed cryo-stage (Fig. 1) is comprised of an isolated sample chamber containing a silver-coated copper-

cooling block. The sample chamber is passively cooled with a constant flow of LN_2 from a dewar and is operated at a stable temperature of $-188°C$ at the sample position. The dewar is also fitted with a dry nitrogen gas purging system. This is used for purging of the cryo-stage with N_2 gas, heated to 60°C with an external gas heater, to remove residual humidity within the system in preparation for the next session. During cooling, a slight overpressure of cold N_2 gas in the chamber prevents atmospheric air to condense on the sample and contaminate it with frost. The cold sample chamber is separated by a 170 μm thick, gold-coated, cover glass from the microscope chamber, which is kept at ambient temperatures. The gold coating reflects infrared photons during imaging, therefore decreasing sample heating. To increase stage stability during imaging and to provide better thermal conductivity, the specimen is kept stationary, while the microscope moves underneath the specimen holder. A heated chamber lid with an integrated light-emitting diode provides bright light for transmitted light microscopy. The microscope chamber is constantly purged with dry nitrogen gas to reduce the humidity to roughly 4%, such that frosting of the glass cover slip

separating the objective from the cold sample chamber is minimized.

Plunge frozen grids were fixed into autogrids, mounted and secured into a shuttle system, and sealed with a translucent lid (Fig. S1). This system offers easy and safe handling of the grids during transfers and allows imaging of the grids within the sealed shuttle, thus preventing contamination during imaging (Fig. S2). With this design of stage and shuttle, the samples were kept bellow devitrification temperature during cryo-FLM imaging even though a short-working-distance $40\times$ objective was used, and no sign of devitrification was observed in cryo-TEM (Fig. S3).

A shuttle accommodates two grids, which can be fully imaged within 1.5 h of a cooling period provided by a single LN_2 dewar fill. Refilling of the dewar while the grids are positioned within the chamber was avoided to minimize the risk of introducing frost contamination. Thus, refilling of the dewar was performed during the exchange of samples. Overnight purging of the cryo-stage with 60°C dry N_2 and of the microscope chamber with dry N_2 at room temperature, ensures that up to four shuttles can be imaged during a workday without detectable contamination.

Focal sectioning in light microscopy describes the acquisition of multiple images at different focal planes. Combined, these images define a volume of data, in which a fluorescently labeled feature is localized. Data collection for 3D correlation was done using spinning-disk confocal microscopy with a focus step size of 300 nm. In spinning-disk confocal microscopy, higher SNR is achieved because of lower background noise from out-of-focus fluorescence. However, spinning-disk microscopy requires longer exposure times than in wide-field microscopy to generate sufficient signal. This is not a major concern in cryo-FLM because the sample is immobilized and imaging at cryo-temperatures significantly reduces fluorescence bleaching (13). To minimize inaccuracies because of drift and chromatic aberrations during multichannel acquisition, multicolored fiducials, such as Tetraspeck beads, can be applied to the specimen and used for alignment of the stacks (11).

Fiducial markers for FLM and SEM/FIB microscopy

Fiducial markers are visual reference points for image processing, such as correlation and alignment of two maps from two different imaging systems. The markers should show high image contrast both in light and electron microscopy. This can be achieved by combining fluorescence with a material exhibiting a high specific density, which gives rise to a distinct signal from back-scattered electrons detectable in the SEM. Moreover, they must be of regular shape and large enough to be discernible in topographic views of vitrified samples imaged in SEM and FIB.

Mono-sized ferromagnetic polystyrene beads with a diameter of 1 μm have a 40% iron oxide content cross-linked in the polystyrene matrix. They are consistently spherical in shape and size and exhibit a good signal from back-scattered electrons. Moreover, polystyrene is autofluorescent when excited by green light (Fig. 2 A).
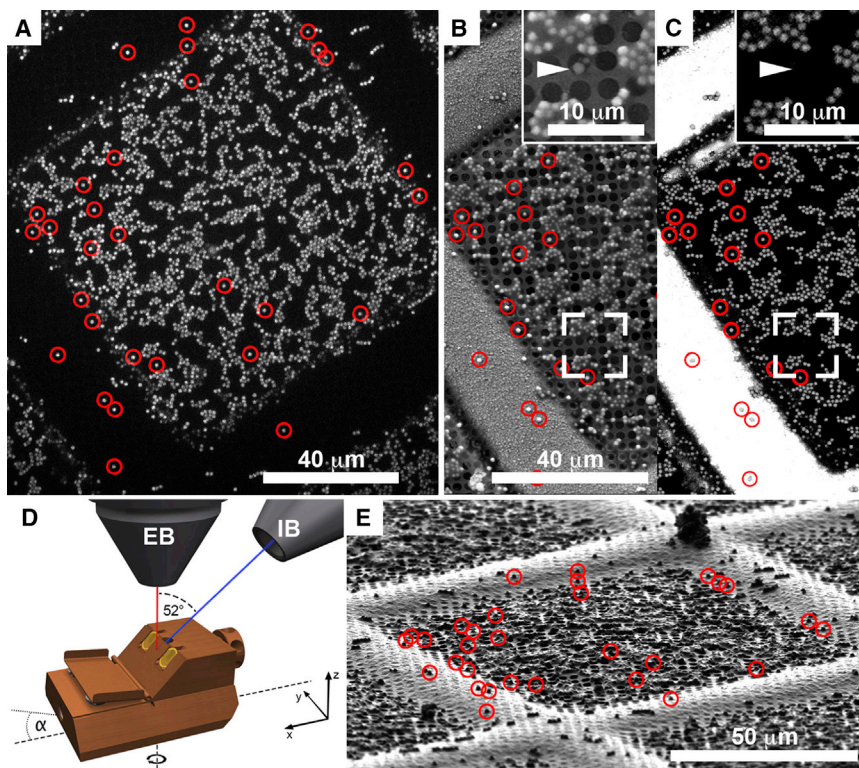

FIGURE 2 Magnetic beads with 1 μm diameter used as fiducial markers for FLM and SEM/FIB correlation. (A) Maximum intensity projection of a spinning-disk confocal stack at an excitation wavelength of 488 nm. Beads are autofluorescent at this wavelength. (B) SE SEM image shows the grid surface topography corresponding to the left half of (A). Inset: higher magnification of area within frame. (C) EBSD SEM image of the same area as in (B). The signal from the iron oxide in the magnetic beads is detectable by the back-scattered electron detector. Inset: magnified view of frame. One ice crystal is marked in the magnified secondary electron image (B) is not visible in the EBSD image (arrowhead). (D). Schematic representation of the SEM/FIB chamber with respect to the FIB shuttle. The FIB shuttle at the grid position has a pretilt of 45°. α, stage tilt. (E) Ion beam view at an angle of 18° with respect to the grid plane (α: 25°). Red circles in (A)–(C) and (E) indicate representative markers used for calculating the correlation accuracy.

The accuracy of the correlation depends on the precision in fitting the centers of the markers. A spherical marker shape is advantageous for a precise determination of its center. Beads of 1 μm diameter were chosen because these were the smallest that could be reliably detected in SEM/FIB (Fig. 2). A pronounced signal in the back-scattered detector allowed unambiguous identification of the fiducial markers and ensured that they were distinguished from ice-crystals or other potential contaminants (Fig. 2, *B* and *C*, *insets*). Single beads are preferred over aggregates because their positions can be precisely identified in both FLM and the SEM/FIB images.

Geometric considerations in the SEM/FIB dual-beam microscope

In the dual-beam microscope, the electron beam and the ion beam are fixed at an angle of 52° with respect to one another. Samples are mounted onto a FIB-shuttle, which accommodates the grids at a pretilt of 45° (Fig. 2 *D*) (7,16). This pretilt allows FIB milling at shallow angles with the ion beam. The close-to-parallel milling geometry is necessary for subsequent observation in the cryo-TEM. The cryo-stage is limited in movement. When cooled, the stage can only tilt in the range of $-5°$ to $+30°$ because of the stiffness of the cooling tubing connected to it (Fig. 2 *D*, α). This prohibits a perpendicular view on the sample with the SEM, which would produce an equivalent view to the FLM image. The FIB view at a typical milling angle (stage tilt of 15° to 25°, corresponding to 7° to 18° with respect to the grid plane) is equivalent to a side view of the FLM volume, corresponds to a viewing angle of 7° to 18° with low axial resolution. Furthermore, the spherical fiducial markers, partially embedded in the thin ice film of cryo-samples, appear as bumps on the surface (Fig. 2 *E*).

Coordinate transformation-based 3D correlation

In a coordinate transformation method, corresponding fiducials are first identified in both the initial and the final imaging system, i.e., spinning-disk confocal fluorescence and SEM/FIB, respectively. For simplicity, from here on we will only refer to correlation between FLM to FIB images. However, all transformations described below are applicable to any final 2D system. The coordinates of the fiducials are used to determine the transformation parameters (e.g., rotation, translation, and scaling) between the two systems. Applying the calculated transformation on the coordinates of an object of interest in the FLM data then yields its position on the FIB image. This position is then targeted in the FIB milling process to capture the structure of interest in a FIB lamella.

A transformation between FLM and FIB imaging modes can be mathematically described by a 3D rigid body transformation together with a scalar (isotropic) scaling. Previously, a correlation approach between 2D fluorescence and

FIB images was developed (21). Because only 2D coordinates had been available, a 2D affine transformation was used to specify the coordinate transformation between the images. Although this transformation provides a good approximation for thin samples, its precision relies on the assumption that all markers and objects of interest lie in the same plane. In the approach presented here, spinning-disk confocal imaging provided additional information in a third dimension (*z*-focal sectioning), which allowed a direct determination of all components of the transformation consisting of 3D rotation, translation, and scaling. However, this 3D transformation could not be determined using the standard 3D optimization in which both initial and final fiducial coordinates are specified in 3D, because FIB images contain only 2D information (22,23). Therefore, the transformation needs to be determined from incomplete data. Nevertheless, the rotation, scale, and one component of translation can be uniquely determined by finding the transformation parameters that minimize the square error, *E*, between the actual FIB coordinates and the transformed fluorescent marker coordinates as follows:

$$E = tr(Y - sRX - d1n)^T(Y - sRX - d1n), \quad (1)$$

where s is the scale factor, R is the rotation, and d is the translation. Here X is a $3 \times n$ matrix and Y is a $2 \times n$ matrix containing coordinates of n markers in confocal and FIB data, respectively, as follows:

$$X = \begin{pmatrix} x_{11} & x_{12} & \dots \\ x_{21} & & \\ x_{31} & & \end{pmatrix}_{3 \times n}, \quad Y = \begin{pmatrix} y_{11} & y_{12} & \dots \\ y_{21} & & \end{pmatrix}_{2 \times n}$$

$$R = \begin{pmatrix} r_{11} & r_{12} & r_{13} \\ r_{21} & \dots & \end{pmatrix}_{2 \times 3}, \quad d = \begin{pmatrix} d_1 \\ d_2 \end{pmatrix},$$

$$1_n = \begin{pmatrix} 1 & 1 & \dots \end{pmatrix}_{2 \times n}. \quad (2)$$

We note that the full 3D rotation matrix contains nine elements and the translation matrix contains three elements, but some components do not enter Eq. 1 because the FIB data is incomplete. The following expression for translation can be derived analytically in the same way as when complete marker coordinates are known:

$$\frac{\partial E}{\partial d} = 0 \Rightarrow d = y^{cm} - sRx^{cm}, \quad (3)$$

where x^{cm} and y^{cm} are the center-of-mass coordinates of FLM and FIB fiducials, respectively. Shifting the fiducial coordinates in both systems to their respective center-of-mass systems removes translation d but otherwise does not modify the error function (Eq. 1).

Next, we parameterized the rotation matrix using the Euler parameters e_0-e_3 (transform-like unit quaternions and closely related to Caley-Klein parameters, but not to

be confused with Euler angles). For completeness, the whole rotation matrix is shown in Eq. 4, but only the first two rows enter the optimization procedure.

$$R = \begin{pmatrix} e_0^2 + e_1^2 - e_2^2 - e_3^2 & 2(e_1e_2 - e_0e_3) & 2(e_1e_3 + e_0e_2) \\ 2(e_1e_2 + e_0e_3) & e_0^2 - e_1^2 + e_2^2 - e_3^2 & 2(e_2e_3 - e_0e_1) \\ 2(e_1e_3 - e_0e_2) & 2(e_2e_3 + e_0e_1) & e_0^2 - e_1^2 - e_2^2 + e_3^2 \end{pmatrix} \tag{4}$$

These parameters are closely related to quaternions, and they are normalized to 1: $e_0^2 + e_1^2 + e_2^2 + e_3^2 = 1$ and provide a proper parameterization of the space of 3D rotations.

We then proceeded to find the optimal values of the scaling and the Euler parameters by numerical optimization of the error function (Eq. 1 where translation is omitted). The optimization is done under the constraints that the Euler parameters are normalized and that the scaling factor is positive. Although formally not necessary, we also included requirements that the Euler parameters are between 0 and 1. The numerical method used is sequential least squares programming, as implemented in the SciPy package (20).

The optimization procedure yielded values for the scale and the Euler parameters. This allowed the calculation of the full (3 × 3) rotation matrix (Eq. 4) and the extraction of Euler angles. Next, two components of translation were calculated (Eq. 3), while the third was not defined and can be temporarily set to 0. Finally, the complete transformation was applied to the fiducials coordinates in the FLM data to obtain the 3D coordinates in the FIB system. By default, we chose the third translation component so that the mean marker z-position in the FIB system is 0. Other choices, such that a particular marker has z-position 0, are also possible. The transformation error was then calculated (Eq. 1). It is not influenced by the choice of the third translation component.

The optimization procedure requires specifying initial values for the scale and the Euler parameters. In some cases, the initial values led to nonoptimal solutions. To eliminate this problem, the optimization procedure is executed multiple times, starting with different initial values. We used three procedures to generate different sets of initial values: 1) randomly generated initial value sets; 2) in case approximate scale and 3D rotations are known, initial value sets were randomly generated in a fixed neighborhood of the approximate values; and 3) the same as for the previous approach, except that the approximate solution is calculated from the marker coordinates. For this last approach, 2D affine transformation is calculated using only x and y coordinates of FLM and FIB markers, as it was done earlier (21). Singular value decomposition of the general linear part of the calculated transformation yields two rotation matrices and two eigenvalues. Angles corresponding to the two rota-

tions represent the first and the third Euler angles in the XZX convention, whereas the two eigenvalues can be converted into the 3D scale and the second Euler angle. Because the second Euler angle can be determined only up to a sign, two sets of initial values are generated. The validity of this approximation is justified by the fact that the extent of fluorescence marker coordinates along the x and y axes is much larger than along the z axis.

This procedure was implemented in the Python programming language. Typically 10 to 20 sets of initial values were used. The optimal solution was reached in all test cases. Computation is fast; hundreds of optimizations could be performed in 1 s on a standard laptop/desktop computer. Because six independent parameters need to be determined and each marker provides two constraints, three noncollinear markers are theoretically sufficient. This procedure showed better convergence than the following two alternative procedures that we also investigated: 1) constrained optimization where the orthonormality was imposed on the six elements of the rotation matrix (Eq. 2); and 2) nonconstrained optimization where the rotation matrix was parametrized by Euler angles.

Accuracy measure of the correlation procedure

We estimated the accuracy of the 3D coordinate transformation by the leave-one-out cross-validation test described by Kukulski et al. (24) and Schrob et al. (12). Following this procedure, coordinate transformation is computed using a subset of fiducial markers, and coordinates of markers not used for correlation are used to determine the deviation of the predicted bead position (from FLM) relative to the true bead position (in the SEM/FIB image), which we define as the error. We employed six data sets in total, containing bead-only data (as shown in Fig. 2) as well as beads in cellular samples (as shown in Fig. 4). All available beads in each data set were selected into a pool, from which we randomly generated data sets with different numbers of markers used for calculating the correlation. Each such experiment was iterated 100 times to generate correlation statistics. Based on these, we determined the errors and correlation accuracy (Fig. 3 and Table 1).

The mean error in x and y, as a function of the number of markers that were used for the correlation, shows that accuracy in the range of tens of nanometers can be achieved with a minimum of four markers (Table 1). This is correct for
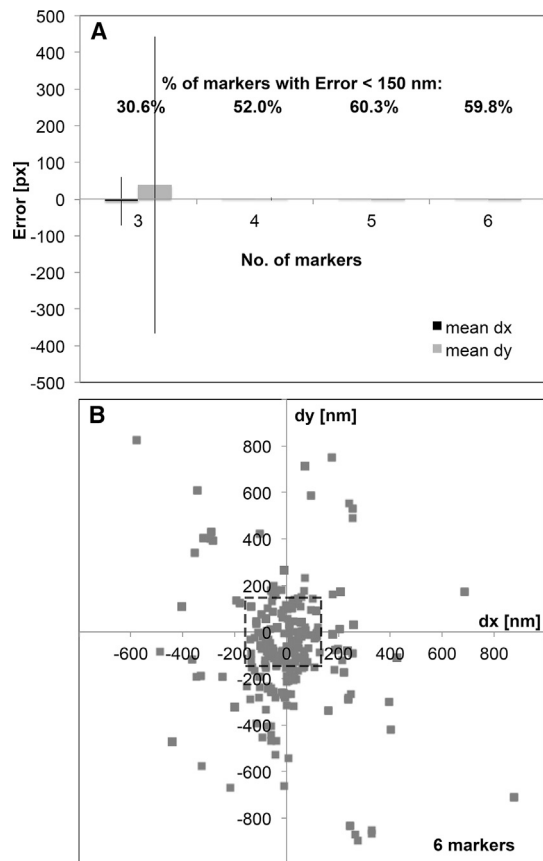
FIGURE 3 Measurement of the correlation accuracy from FLM to FIB. (A) Mean ± SD of deviation from prediction in x and y (error) as a function of the number of markers used for calculating the correlation. px = 161.25 nm. Percentages represent the fraction of markers for which the average deviation was smaller than 150 nm. (B) Scatter plot of errors in x and y when six markers are used for correlation. Almost 60% of the cross-validated markers are localized with an accuracy better than 150 nm (dashed box).

ducials, the standard deviation falls in the range of 200 to 350 nm (Table 1).

Aiming at a final lamella thickness of 300 nm, we set an upper error threshold of 150 nm. With six markers used for correlation, ~60% of the calculated deviations in the FLM-to-FIB data fall within a range of ± 150 nm. Thus, the achieved correlation accuracy provides a realistic range for producing targeted samples for cryo-ET using FIB milling.

3D correlative workflow applied to cellular samples

The developed correlative procedure was applied to vitrified HeLa cell cultures (a detailed protocol of the workflow is provided in Table S1). Fluorescent dyes specifically targeting lipid droplets (LDs) were added to wild-type HeLa cells, synchronized in mitosis. LDs are organelles of all eukaryotic cells, which function primarily as a depot of neutral lipids and have a fundamental role in metabolism and cellular homeostasis. Most importantly for the application presented here, they are spherical in shape, 200 to 800 nm in diameter, and highly electron dense when observed by cryo-TEM. They are thus easily distinguishable in cellular FIB lamellas. We applied two fluorescence dyes targeting nonspecific neutral lipids (green fluorescence) and specific fatty acids (red fluorescence). Magnetic beads (green fluorescence) were applied to the grids before vitrification. Spinning-disk confocal stacks were acquired for cells of interest (Fig. 4 A).

We performed a 3D correlation as described above to this data set using eight beads as fiducial markers clearly distinguishable in the FLM and FIB data (Fig. 4, A and B, respectively, red circles). The estimated correlation mean error ± SD were 53.44 ± 91.05 for FLM to FIB and 46.17 ± 83.85 nm for FLM to SEM (using 12 fiducials).

A thin lamella was produced by FIB milling after correlation (Fig. 4, C and D) to target an agglomerate of LDs (Fig. 4 A, frame) and was subsequently observed by cryo-TEM (Fig. 4 E). Round electron dense particles are

both FLM-to-FIB correlation and FLM-to-SEM correlation, and is necessary for targeting specific structures in lamellas to be used for cryo-TEM observations. Correlation accuracy increases with larger number of fiducials, and the standard deviation of the error decreases. However, even with six fi-

TABLE 1 Measurement of the Correlation Accuracy

No. of Markers	3	4	5	6
FLM to SEM				
Mean dx ± SD (nm)	−126.11 ± 5290.21	24.05 ± 729.93	13.51 ± 301.96	20.12 ± 225.49
Mean dy ± SD (nm)	737.57 ± 12,024.02	60.14 ± 1212.59	11.80 ± 487.86	12.25 ± 341.44
% dx < 150 nm	43.71	55.71	60.43	62.71
% dy < 150 nm	22.71	46.00	58.00	61.86
FLM to FIB				
Mean dx ± SD (nm)	−993.77 ± 10704.17	6.85 ± 351.91	23.07 ± 235.62	12.06 ± 209.52
Mean dy ± SD (nm)	6135.44 ± 65,197.48	5.70 ± 614.66	−27.65 ± 306.38	−23.48 ± 272.69
% dx < 150 nm	41.20	54.80	62.00	60.60
% dy < 150 nm	20.00	49.20	58.60	59.00

Mean ± SD of deviation from prediction in x and y, as a function of the number of markers used for calculating the correlation from FLM to SEM (top) and FLM to FIB (bottom), and the fraction of markers with deviations smaller than 150 nm.
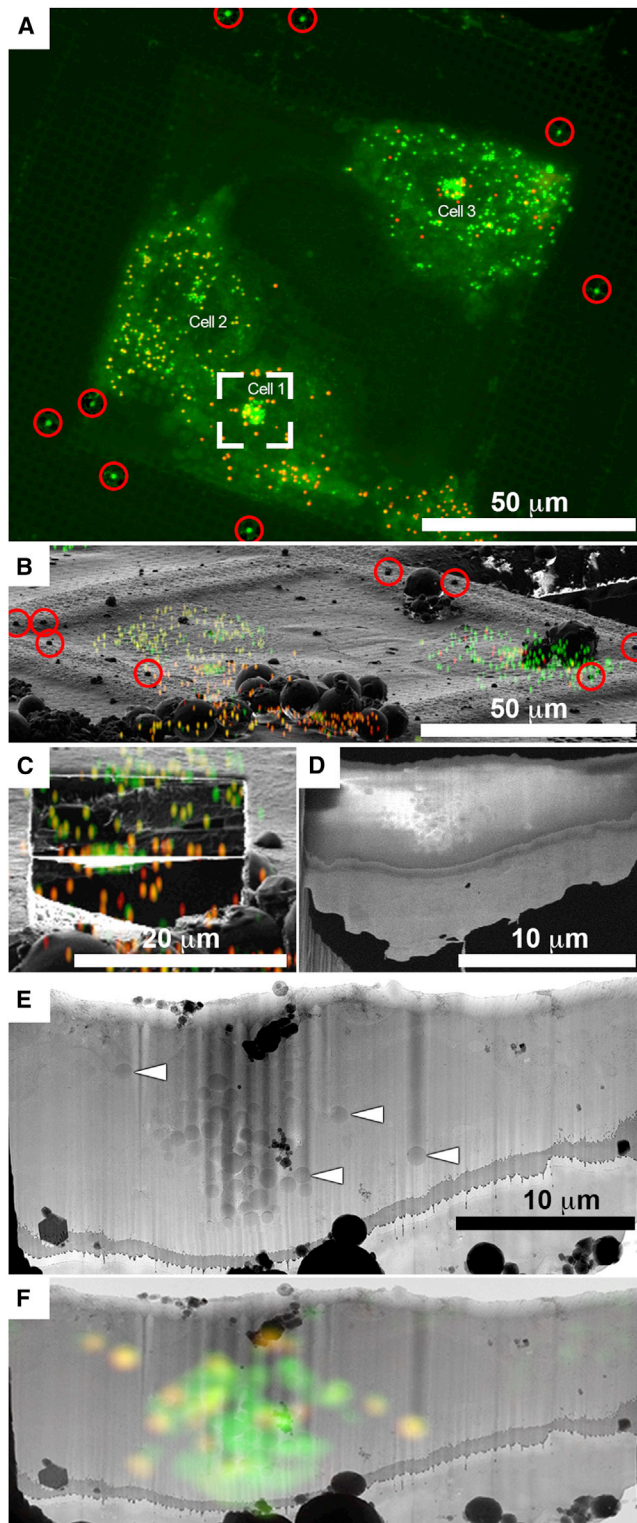
FIGURE 4 Three-dimensional correlation applied to synchronized HeLa cell culture for targeting fluorescently labeled lipid droplets. (*A*) Maximum intensity projection of the spinning-disk confocal volume. Green shows general neutral lipid droplets dye and magnetic beads used as fiducials (levels were adjusted separately inside red circles for better visualization of the fiducials). Red shows neutral fatty acids dye. (*B*) FIB image at the same sample position overlaid with FLM data after applying transforma-tion. Three-dimensional correlation was performed with the encircled eight beads in (*A*) and (*B*). (*C* and *D*) A thin lamella was produced by FIB milling. (*C*) FIB view overlaid with FLM data after applying transformation. (*D*) SEM top view. (*E*) Cryo-TEM montage of lamella. Lamella orientation as in (*D*). Arrowheads indicate some of the electron dense LDs. (*F*) Overlay of cryo-TEM montage of lamella with a computer-generated oblique slice through the confocal volume. LDs stained in green or red are distinguish-able within the lamella.

observed throughout the lamella and are especially promi-nent as an agglomerate at the center (Fig. 4 *E*, *arrowheads*). A second correlation step was performed to navigate acqui-sition of cryo-TEM data at fluorescently labeled positions within the lamella. This required correlation between the original spinning-disk confocal fluorescence volume and the TEM montage. To do this, a FIB image of the final lamella (including the fiducials originally used for the corre-lation), is used to retrieve the actual final lamella position within the fluorescence volume. The fluorescence volume is deconvolved to reduce the influence of the PSF. Then a slice through the fluorescence volume is computationally extracted at this position. The slice, typically two pixels in thickness corresponding to roughly 300 nm (the lamella thickness) is transformed using calculations based on the fi-ducials to fit the SEM view of the final lamella. Finally, the TEM montage of the lamella is correlated in 2D to the SEM image of the final lamella based on features at the edges of the lamella. The 2D correlation was produced using the three-point correlation function in the MAPS software. This allows superimposing the fluorescence oblique slice onto the lamella TEM montage and to identify fluorescently labeled objects within the montage. The fluorescence signal correlated well with the high-electron-density LDs observed in the TEM, and the overlay of the two data sets (Fig. 4 *F*) clearly showed the position of LDs stained nonspecifically with the general dye (*green*) and those specifically stained for fatty acids (*red*).

DISCUSSION

Electron-transparent lamellas amenable for high-resolution cryo-ET analysis can now be routinely produced in biolog-ical samples (25,26). To specifically capture a low-abun-dance and dynamic fluorescently labeled intracellular structure in cryo-ET, we have developed a procedure to direct FIB milling so that the structure of interest is retained in the sample while the surrounding material is removed. The procedure is incorporated into the sample preparation workflow for molecular structural biology in situ (7). We show that the new cryo-stage, mounted on top of a modular light microscope, permits the use of low working distance air objectives with higher NA (0.9). This allows for higher-resolution imaging and, importantly, spinning-disk confocal microscopy for *z*-sectioning. This produced 3D volumes in which the coordinates of structures of interest could be defined in all dimensions.

Despite the low distance between the ambient temperature objective and the sample kept at liquid nitrogen temperatures, no devitrification of the sample was detected (Fig. S3). The passive cooling system ensures that sample drift and vibrations are minimal during imaging.

Although a higher lateral resolution is obtained by using higher NA objectives, the resolution in *z* is still limited. Higher resolution and better SNR, comparable with room temperature observations employing immersion objectives, would only be possible with cryo-immersion objectives. Nevertheless, by introducing fiducial markers for the 3D correlation, the FLM resolution does not limit the accuracy of the correlation. The correlation accuracy depends on the ability to precisely fit the centers of fiducial markers in all imaging modalities. Clearly, markers need to be visible in both the light and SEM/FIB. We show that polystyrene beads with an iron oxide content of 40% can be detected in both the light microscope (autofluorescence) and the electron microscope (assisted by EBSD). Chemical conjugation of a fluorophore to the magnetic beads would deliver a stronger and more easily distinguishable signal at any desirable wavelength in the fluorescence microscope. We used beads with diameter of 1 μm because beads introduced before plunge freezing are embedded in the vitreous ice. Smaller beads would allow for higher correlation accuracy but they would not be easily detected on the sample surface when imaged in the SEM/FIB.

We tackle the computational 3D correlation problem using coordinate transformation. 3D coordinates of fiducial markers are extracted semiautomatically from the confocal volume with FIJI's 3D Object Counter. Two-dimensional coordinates of fiducial markers are extracted from the SEM or FIB images manually. Errors in these steps will decrease the correlation accuracy.

Site-specific FIB milling of intracellular structures necessitates accurate correlation, in the range of 100 nm. We showed that as low as four fiducial markers are sufficient to obtain mean correlation accuracy on the scale of tens of nanometers. However, the error range remains large (up to 1 μm, Table 1). More markers provide higher correlation accuracy and reduce the error range to 200 to 300 nm. Considering that lamellas prepared for cryo-ET are typically 200 to 300 nm thick, the current estimated accuracy is sufficient to allow site-specific milling of biological samples in 60% of the times. This estimate is based on our error calculations on the full raw data, in which all fiducials in a given data set are used and in which outliers contribute to large SD. Outlier fiducials may arise from inaccurate manual picking of the fiducials or from local deformations of the sample during transfers. Optimization of the correlation procedure can be achieved by avoiding fiducials with high deviations compared with the mean using error minimization procedures.

The correlation accuracy was higher for the cellular samples because we used a larger number of fiducials (8–12) and considered areas where the grid support was completely intact, thus avoiding mechanical deformations that could be generated during transfers from the cryo-FLM to the SEM/FIB. Thus, the precision of targeted-FIB milling process, i.e., retention of selected structures in 300 nm lamellas, will also depend on factors not related to the correlation calculations. These are mainly related to the quality of the sample grids and the stability of the stage in the SEM/FIB. High precision using our procedure can only be achieved when a sufficient number of markers are available for correlation and are clearly distinguishable also in the shallow-angle view of the FIB image, the grid support at the area of interest is intact and does not deform during transfers, and the stage in the SEM/FIB instrument is stable enough to avoid drift during the milling process.

The FLM volume, transformed after correlation, can be precisely superimposed onto the TEM montage of the lamella to navigate the acquisition of cryo-TEM data at fluorescently labeled positions. This allows identification and localization of the fluorescently labeled structures in cryo-tomograms. However, unambiguous identification of sub-diffraction-limit-sized structures within the FIB lamella is still limited by the achievable resolution in FLM. Here, application of superresolution fluorescence light microscopy at cryogenic temperatures, such as demonstrated with single-molecule localization microscopy (27) and photoactivated localizations microscopy (28), would be required.

SUPPORTING MATERIAL

AUTHOR CONTRIBUTIONS

J.M., A.d.M., W.B., and J.P. designed research. J.A., J.M., A.d.M., and V.L. performed research. J.J.F., T.L., and T.M. contributed analytic tools. J.M., J.A., V.L., A.H., W.B., and J.P. wrote the manuscript.

ACKNOWLEDGMENTS

REFERENCES

1. Mahamid, J., and W. Baumeister. 2012. Cryo-electron tomography: the realization of a vision. *Microsc. Microanal.* 26:45–48.

2. Dubochet, J., M. Adrian, …, P. Schultz. 1988. Cryo-electron microscopy of vitrified specimens. *Q. Rev. Biophys.* 21:129–228.

3. Lucić, V., F. Förster, and W. Baumeister. 2005. Structural studies by electron tomography: from cells to molecules. *Annu. Rev. Biochem.* 74:833–865.

4. Hsieh, C., T. Schmelzer, …, M. Marko. 2014. Practical workflow for cryo focused-ion-beam milling of tissues and cells for cryo-TEM tomography. *J. Struct. Biol.* 185:32–41.

5. Mahamid, J., R. Schampers, …, J. M. Plitzko. 2015. A focused ion beam milling and lift-out approach for site-specific preparation of frozen-hydrated lamellas from multicellular organisms. *J. Struct. Biol.* 192:262–269.

6. Marko, M., C. Hsieh, …, C. Mannella. 2007. Focused-ion-beam thinning of frozen-hydrated biological specimens for cryo-electron microscopy. *Nat. Methods.* 4:215–217.

7. Rigort, A., F. J. B. Bäuerlein, …, J. M. Plitzko. 2010. Micromachining tools and correlative approaches for cellular cryo-electron tomography. *J. Struct. Biol.* 172:169–179.

8. Agronskaia, A. V., J. A. Valentijn, …, H. C. Gerritsen. 2008. Integrated fluorescence and transmission electron microscopy. *J. Struct. Biol.* 164:183–189.

9. Sartori, A., R. Gatz, …, J. M. Plitzko. 2007. Correlative microscopy: bridging the gap between fluorescence light microscopy and cryo-electron tomography. *J. Struct. Biol.* 160:135–145.

10. Briegel, A., S. Chen, …, G. J. Jensen. 2010. Correlated light and electron cryo-microscopy. *Methods Enzymol.* 481:317–341.

11. Schellenberger, P., R. Kaufmann, …, K. Grünewald. 2014. High-precision correlative fluorescence and electron cryo microscopy using two independent alignment markers. *Ultramicroscopy.* 143:41–51.

12. Schorb, M., and J. A. G. Briggs. 2014. Correlated cryo-fluorescence and cryo-electron microscopy with high spatial precision and improved sensitivity. *Ultramicroscopy.* 143:24–32.

13. Schwartz, C. L., V. I. Sarbash, …, D. Nicastro. 2007. Cryo-fluorescence microscopy facilitates correlations between light and cryo-electron microscopy and reduces the rate of photobleaching. *J. Microsc.* 227:98–109.

14. van Driel, L. F., J. A. Valentijn, …, A. J. Koster. 2009. Tools for correlative cryo-fluorescence microscopy and cryo-electron tomography applied to whole mitochondria in human endothelial cells. *Eur. J. Cell Biol.* 88:669–684.

15. Le Gros, M. A., G. McDermott, …, C. A. Larabell. 2009. High-aperture cryogenic light microscopy. *J. Microsc.* 235:1–8.

16. Rigort, A., F. Bäuerlein, …, J. M. Plitzko. 2010. A 360° rotatable cryo-FIB stage for micromachining frozen-hydrated specimens for cryo-electron tomography. *Microsc. Microanal.* 16 (S2):220–221.

17. Mastronarde, D. N. 2005. Automated electron microscope tomography using robust prediction of specimen movements. *J. Struct. Biol.* 152:36–51.

18. Schindelin, J., I. Arganda-Carreras, …, A. Cardona. 2012. Fiji: an open-source platform for biological-image analysis. *Nat. Methods.* 9:676–682.

19. Bolte, S., and F. P. Cordelières. 2006. A guided tour into subcellular co-localization analysis in light microscopy. *J. Microsc.* 224:213–232.

20. Jones, E., T. Oliphant, and P. Peterson. 2001. SciPy: open source scientific tools for Python. http://www.scipy.org/.

21. Fukuda, Y., N. Schrod, …, V. Lucic. 2014. Coordinate transformation based cryo-correlative methods for electron tomography and focused ion beam milling. *Ultramicroscopy.* 143:15–23.

22. Myronenko, A., and X. Song. 2009. On the closed-form solution of the rotation matrix arising in computer vision problems. Preprint, submitted April 9, 2009. http://arxiv.org/abs/0904.1613.

23. Umeyama, S. 1991. Least-squares estimation of transform parameters between two point patterns. *IEEE Trans. Pattern Anal. Mach. Intell.* 13:376–380.

24. Kukulski, W., M. Schorb, …, J. A. G. Briggs. 2012. Precise, correlated fluorescence microscopy and electron tomography of lowicryl sections using fluorescent fiducial markers. *Methods Cell Biol.* 111:235–257.

25. Rigort, A., F. J. B. Bäuerlein, …, J. M. Plitzko. 2012. Focused ion beam micromachining of eukaryotic cells for cryoelectron tomography. *Proc. Natl. Acad. Sci. USA.* 109:4449–4454.

26. Villa, E., M. Schaffer, …, W. Baumeister. 2013. Opening windows into the cell: focused-ion-beam milling for cryo-electron tomography. *Curr. Opin. Struct. Biol.* 23:771–777.

27. Kaufmann, R., P. Schellenberger, …, K. Grünewald. 2014. Super-resolution microscopy using standard fluorescent proteins in intact cells under cryo-conditions. *Nano Lett.* 14:4171–4175.

28. Chang, Y. W., S. Chen, …, G. J. Jensen. 2014. Correlated cryogenic photoactivated localization microscopy and cryo-electron tomography. *Nat. Methods.* 11:737–739.